The Electrochemical Society
Advancing solid state & electrochemical science & technology

Influence of Rutile and Anatase TiO$_2$ Precursors on the Synthesis of a Li$_{1.5}$Al$_{0.5}$Ti$_{1.5}$(PO$_4$)$_3$ Electrolyte for Solid-State Lithium Batteries

View the article online for updates and enhancements.

Influence of Rutile and Anatase TiO$_2$ Precursors on the Synthesis of a Li$_{1.5}$Al$_{0.5}$Ti$_{1.5}$(PO$_4$)$_3$ Electrolyte for Solid-State Lithium Batteries

Andrea La Monaca,[1,2] Wen Zhu,[1] Zimin Feng,[1] Giovanni Bertoni,[3]
Daniele Campanella,[1] Gabriel Girard,[1] Sylvio Savoie,[1] Alina Gheorghe Nita,[1]
Daniel Clement,[1] Hendrix Demers,[1] Ashok Vijh,[1] Federico Rosei,[2] and Andrea Paolella[1,z]

[1]*Centre d'Excellence en Électrification des Transports et Stockage d'Energie, Hydro-Québec, Varennes, Québec J3X 1S1, Canada*
[2]*Centre Énergie, Matériaux et Télécommunications, Institut National de la Recherche Scientifique, Varennes, Québec J3X 1P7, Canada*
[3]*Istituto Nanoscienze, Consiglio Nazionale delle Ricerche, 41125 Modena, Italy*

We report the effect of using rutile and anatase TiO$_2$ as precursors in the synthesis of ceramic Li$_{1.3}$Al$_{0.3}$Ti$_{1.7}$(PO$_4$)$_3$ (LATP) NASICON-type electrolyte for solid-state lithium batteries. Anatase TiO$_2$ enables LATP crystallization at lower temperatures while rutile TiO$_2$ leads to a purer and more crystalline LATP phase. We believe these findings are an important contribution towards the development of more effective and less expensive synthesis of Ti-based solid electrolyte materials.
© 2022 The Electrochemical Society ("ECS"). Published on behalf of IOP Publishing Limited. [DOI: 10.1149/1945-7111/ac6325]

The ever-growing demand for efficient energy storage devices (batteries in particular) observed in the last decades requires a prompt introduction of a breakthrough technology. Lithium-ion batteries (LIBs), ubiquitous in portable computing technology, are currently struggling to provide the energy density required for automotive applications, thus limiting the widespread development of electric vehicles.[1–4] The gravimetric energy density of a commercial LIB corresponds to 160–260 Wh kg^{-1},[4] around a hundred times lower than gasoline (12700 Wh kg^{-1}). Although research efforts aim to reach values higher than 350 Wh kg^{-1} by 2050 thanks to the potential use of high-voltage cathode materials,[4] it is evident that the technology itself is reaching its intrinsic limits.[5] Moreover, the inherent safety issues related to the use of organic liquid electrolyte, which involve flammability and potential explosion, are still a major concern.[6] Hence, among the best candidates to replace or at least complement LIBs all-solid-state lithium batteries (ASSLBs) are being studied intensively. Replacing flammable liquid media, usually featured in LIBs, with an inorganic solid electrolyte (ISE) enables the use of metallic lithium as anode, thus boosting the energy density of the device.[7] However, the ultimate ISE is still elusive. Few ceramic materials proposed thus far display a suitable ionic conductivity, while several are characterized by chemical, electrochemical or thermal instabilities.[8–10] Hence, major efforts must be invested into the optimization of already known materials. One of the most promising is the NASICON-like Al-doped LiTi$_2$(PO$_4$)$_3$ (LATP) which presents an ionic conductivity of the order of 10^{-4} S cm^{-1}, while being chemically stable in ambient conditions.[11–13] The aliovalent substitution of Ti^{4+} by Al^{3+} is crucial for increasing Li ions concentration and mobility, thus improving the conductivity of the material.[8] Moreover, it can be synthesized starting from relatively inexpensive precursor materials through different processes. A facile method to synthesize NASICON-like LATP is by a solid-state approach, which consists in mixing oxide-based precursor materials and alternate ball-milling and high temperature steps until achieving a high purity phase. This class of synthesis methods is characterized by complicated and expensive steps; hence they are considered less suitable for industrial mass production. It is thus very desirable to optimize the procedures for a more efficient synthesis.[14,15]

In this work, we studied how different polymorphs of TiO$_2$ can affect the synthesis and the properties of Li$_{1.5}$Al$_{0.5}$Ti$_{1.5}$(PO$_4$)$_3$ (LATP) electrolyte. Specifically, we synthesized LATP by a solid-state method using anatase TiO$_2$ as Ti source, and hereafter referred to as aLATP. We replicated the same synthesis except using rutile TiO$_2$ instead (the final product denoted rLATP). We studied the crystallization of both materials using in situ high-temperature X-ray diffraction (HTXRD). By combining HTXRD data, scanning electron microscopy (SEM) images, high-resolution transmission electron microscopy (HRTEM) and electrochemical impedance spectroscopy (EIS) results, we evaluated the influence of the two phases of TiO$_2$ on the synthesis, and on the properties and performance of the synthesized LATP electrolytes.

Experimental

Materials and methods.—Lithium carbonate (Li$_2$CO$_3$), aluminum oxide (Al$_2$O$_3$), ammonium phosphate dibasic ((NH$_4$)$_2$HPO$_4$), rutile and anatase titanium oxide (TiO$_2$) were purchased from Sigma Aldrich. In a standard solid-state synthesis, stoichiometric amounts of Li$_2$CO$_3$, Al$_2$O$_3$, TiO$_2$, and (NH$_4$)$_2$HPO$_4$ were placed in a zirconia vial together with four zirconia balls (diameter: 12.7 mm) and ball milled in a SPEX mixer for 15 min. The fine powder was then heated in an alumina crucible at 550 °C for 2 h and subsequently at 700 °C for 2 h with a heating rate of 5 °C min^{-1} in air atmosphere.

Characterizations.—The morphological characterization was carried out using a Lyra 3 scanning electron microscope (SEM) by Tescan. Elemental composition analysis was performed using a windowless energy dispersive spectrometer (EDS) Extreme by Oxford instruments. To acquire cross section SEM images, pellets have been prepared with an Ar Ion Milling IM4000 Plus (Hitachi), using a 6 kV ion beam energy and a fast 30° rotation for 4 h.

HRTEM images were acquired using a transmission electron microscope (Thermo-Fischer Scientific Talos 200 S) at 200 kV incident energy. EDS maps and high angle annular dark field images (HAADF) were acquired in scanning mode (STEM). Prior to the analysis, aLATP and rLATP powders were dispersed in ethanol and drop-casted on holey carbon films on copper grids.

X-ray diffraction was performed using a high temperature X-ray diffractometer (HTXRD) by Rigaku, equipped with a CuK$_\alpha$ radiation source. A mixture of Li$_2$CO$_3$, Al$_2$O$_3$, TiO$_2$, and (NH$_4$)$_2$HPO$_4$

was heated at 3 °C min^{-1} from room temperature to 700 °C (dwelling time: 2 h) in ambient atmosphere. Scanning was performed in 0.04° steps at a 6.14° min^{-1} rate.

Electrochemical impedance spectroscopy (EIS) was carried out using a BioLogic VMP potentiostat/galvanostat by applying an AC perturbation of 5 mV in a frequency range of 1 MHz–50 mHz from 20 °C to 80 °C. Prior to EIS measurements, pellets have been prepared by hot-pressing 0.75 g of LATP powders at 56 MPa and 750 °C for 1 h between graphite foils using a titanium-zirconium-molybdenum die. They were then placed between stainless steel blocking electrodes in 2032-type coin cells.

Density values of aLATP and rLATP hot-pressed pellets were calculated using the following equation:

$$d(\%) = \left(\frac{wv}{d_{th}}\right) \times 100$$

where w and v are the weight and the volume of the sample respectively, and d_{th} is the theoretical density of LATP (estimated to be equal to 2.9 g cm^{-3}).

Results and Discussion

SEM imaging was used to investigate the morphology of rLATP and aLATP (Fig. 1). Both samples consist of cubic and irregular crystallites, which tend to form agglomerates of several microns in size. The irregular shape is related to the temperature used for the synthesis, i.e. 700 °C.[16,17] When a temperature of 950 °C is used, resulting crystals are predominantly cubic shaped in both samples (Fig. S1 (available online at stacks.iop.org/JES/169/040515/mmedia)). EDS analysis of both samples confirmed the formation of LATP with an even elemental distribution without apparent segregation of secondary phases.

HRTEM images were acquired to evaluate the structure of single LATP grains and to better characterize their boundary composition. Figures 2a and 2b report the HRTEM images of a single crystallite of both aLATP and rLATP, with the corresponding fast Fourier transform (FFT) pattern in the inset. Both samples are characterized by the typical rhombohedral structure of the NASICON phase (space group R$\bar{3}$c). It should be noted that due to electron diffraction, some reflections that are expected to be weak or forbidden in pure kinematic approximation are visible, such as (0,1,1) and (0,−1,1) at ∼0.70 nm. Figures 2c and 2d display STEM-HAADF images and STEM-EDS elemental maps acquired on both aLATP and rLATP samples. All the elements, i.e. Ti, Al, P, and O result homogeneously distributed without any evidence of segregation at boundaries, thus confirming the results of the SEM-EDS analysis.

HTXRD has been performed on both samples to have a deep insight on LATP crystallization and how it is influenced by the presence of rutile and anatase phases. The evolutions of XRD patterns of both samples are displayed in Figs. 3a and 3b. The initial XRD patterns differ because of the Ti precursor used (Fig. S2). When the temperature increases, the XRD patterns of both samples evolve: the peaks ascribed to intermediate product, such as Li$_3$PO$_4$ and biphosphammite (NH$_4$)H$_2$PO$_4$ start to appear between 100 °C and 200 °C in the patterns of both samples. Then, peaks corresponding to precursor materials, rutile and anatase included, start to decrease in intensity and LATP rhombohedral phase appears. Specifically, in the diffractogram of aLATP acquired at 378 °C, peaks corresponding to the NASICON phase (space group R$\bar{3}$c) of Li$_{1.2}$Al$_{0.2}$Ti$_{1.8}$(PO$_4$)$_3$ (PDF card: 01–084–5450) started appearing. In a similar temperature range, no peaks are detected in the rLATP pattern, as displayed in Fig. 4a. When the temperature reaches 583 °C, we observed the appearance of the LATP phase also in the rLATP pattern, while in the aLATP pattern collected in the 592 °C–622 °C range the corresponding peaks are already very intense (Fig. 4b). When the temperature reached 700 °C, aLATP phase is characterized by a higher degree of crystallinity and less impurity phases than rLATP. However, after dwelling at 700 °C for 2 h, rLATP become
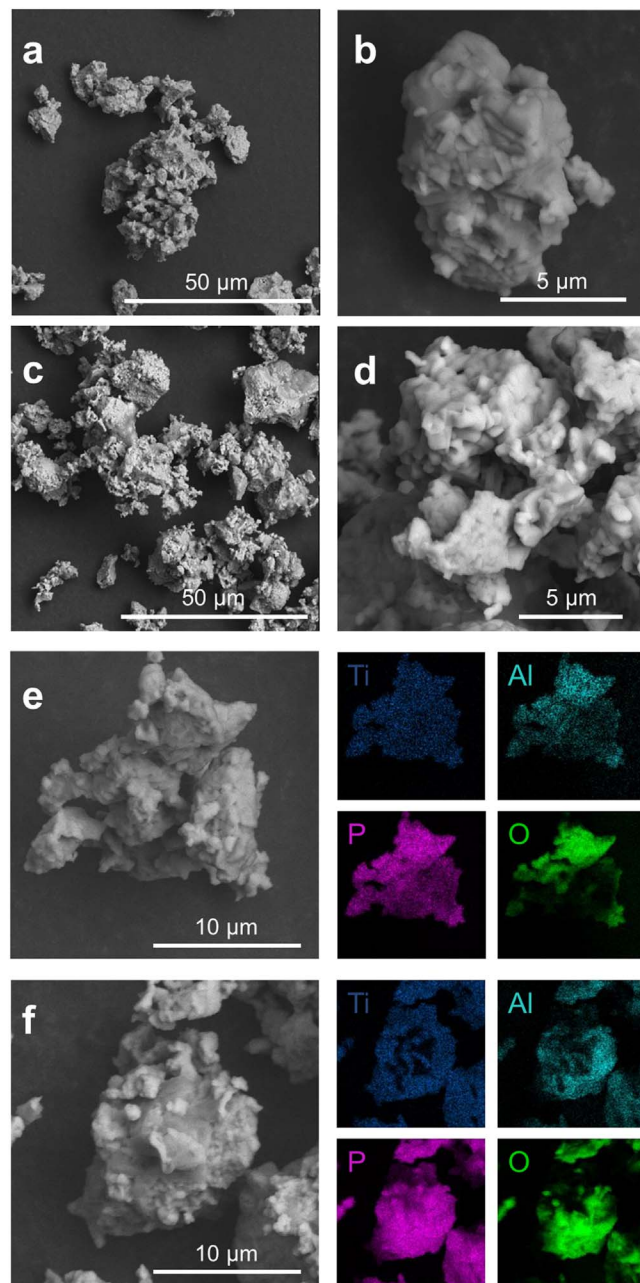

Figure 1. SEM images of (a), (b) aLATP and (c), (d) rLATP particles acquired at different magnifications. SEM-EDS analysis and corresponding elemental mapping of (e) aLATP and (f) rLATP.

purer and more crystalline, displaying only a few low-intensity peaks ascribable to Li$_4$P$_2$O$_7$ and Li$_3$PO$_4$ while, several peaks associated with AlPO$_4$ and Li$_4$P$_2$O$_7$ have been identified in the aLATP diffractogram acquired after the 2 h dwelling at 700 °C (Fig. S3). Both samples were cooled down to room temperature for the final XRD analyses. The patterns did not change significantly from their 700 °C counterparts, and this verifies their stability (Fig. S3). At 300 °C, only TiO$_2$ XRD patterns appear in the samples. This indicates that at 300 °C all the precursors have become amorphous except for TiO$_2$, and that TiO$_2$ is the last one to react (Fig. S4). The use of anatase or rutile phase of TiO$_2$ does not affect the reaction routes of the synthesis. Between 127 °C–327 °C, the formation enthalpy and Gibbs energy of anatase TiO$_2$ are about 6.2 kJ mol^{-1} higher than those of rutile TiO$_2$.[18] Assuming an Arrhenius-type reaction rate, this difference causes a four-fold faster kinetics for anatase TiO$_2$ reactions at 327 °C, in good agreement with our
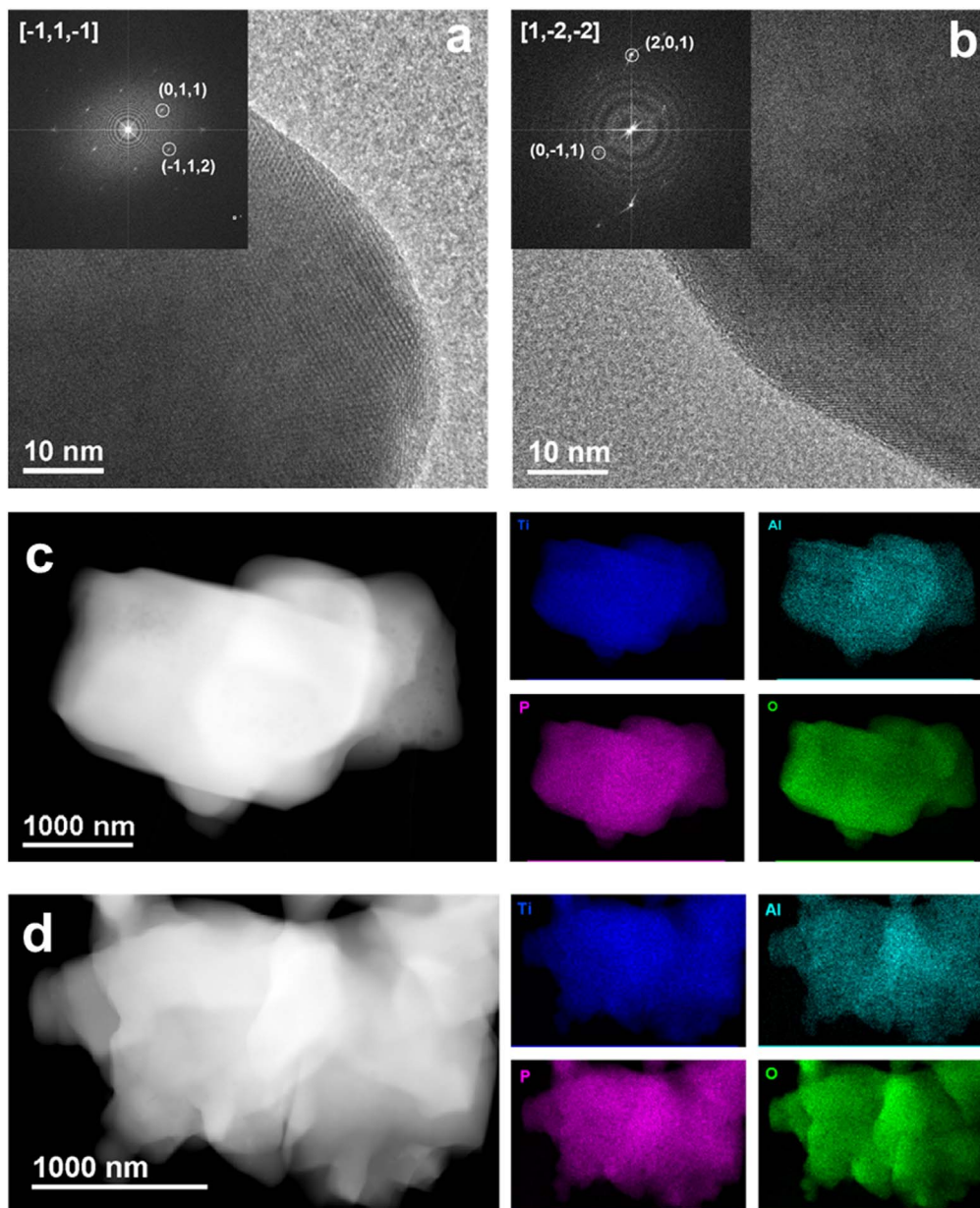
Figure 2. HRTEM images of (a) aLATP and (b) rLATP crystallites with corresponding FFT patterns in the insets. STEM-HAADF images and corresponding STEM-EDS elemental maps of (c) aLATP and (d) rLATP.
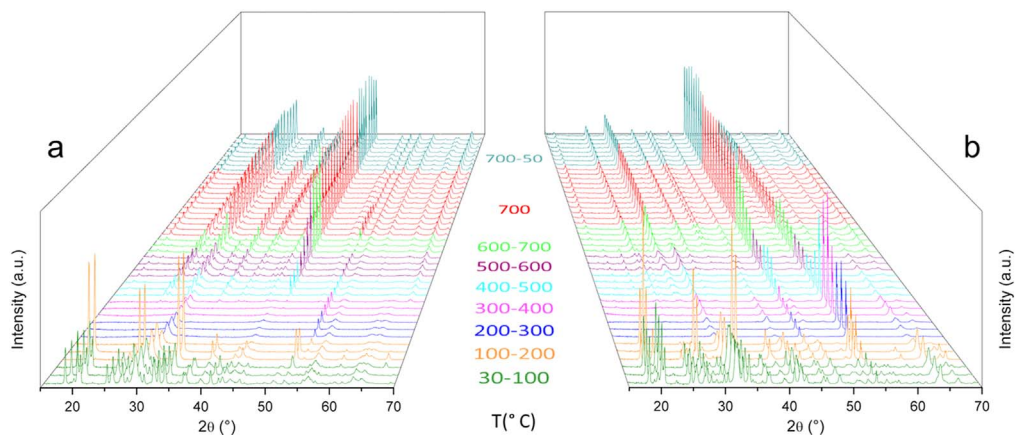

Figure 3. HTXRD analyses of (a) aLATP and (b) rLATP performed in a temperature range of 30 °C–700 °C with a dwell time of 2 h. XRD patterns acquired while cooling down the samples from 700 °C to 50 °C are displayed too.
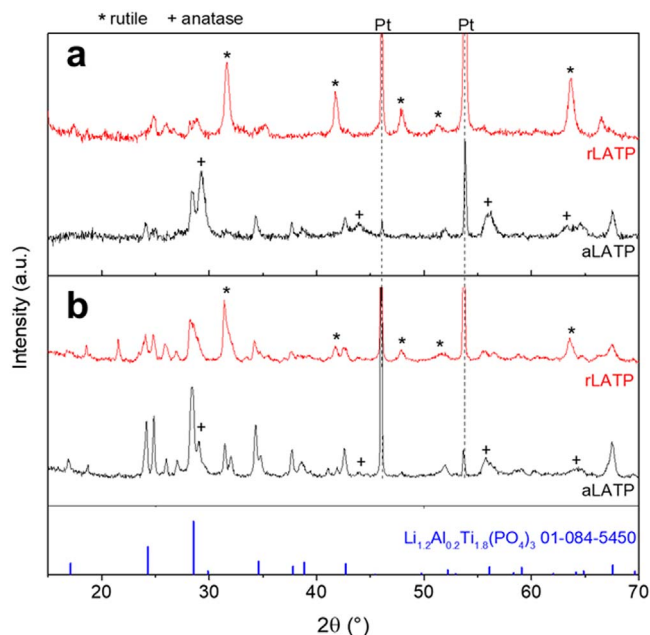
Figure 4. XRD patterns acquired in a temperature range of (a) 378 °C–408 °C for aLATP and 370 °C–400 °C for rLATP, and (b) 592 °C–622 °C for aLATP and 583 °C–613 °C for rLATP. ((*): TiO$_2$ rutile; (+): TiO$_2$ anatase; Pt peaks derive from the crucible).

observation that LATP appears sooner with anatase TiO$_2$ than with rutile TiO$_2$.

We also performed SEM analyses of anatase and rutile TiO$_2$ precursors to evaluate the potential effect of their morphology on the crystallization mechanism of LATP. The acquired images are displayed in Figs. S5a and S5b. While anatase TiO$_2$ features some relatively large crystals, in the order of few microns, the dimensions of most of the crystallites of both precursor materials appear to be in the nanometric order, thus excluding any possible size-related effect on LATP synthesis. The XRD patterns of anatase and rutile TiO$_2$ (Fig. S5c) confirmed the morphological results. By using the Scherrer equation, the average size of crystallites resulted 100 and 460 Å, for anatase and rutile TiO$_2$, respectively. This leads to the conclusion that the different reactivity is based only on thermo-dynamical grounds.

Pellets have been prepared with both aLATP and rLATP by hot-pressing the corresponding powders at 750 °C under 56 MPa. The density of both aLATP and rLATP pellets, estimated by using their weight and dimensions, resulted equal to 90% of the theoretical value. To evaluate the ionic conductivity, each sample has been painted with silver ink and placed in a coin cell between stainless steel blocking electrodes (Fig. 5a). EIS spectra were acquired in the

20 °C–80 °C temperature range. The resulting Nyquist plots consist of two semicircles: the first one was acquired at high frequency, while the second one, can be observed in the mid-low frequency region and appears small and partly convoluted with the double layer capacitance arising at the electrodes. Similar findings were reported for hot-pressed LLZO by Tenhaeff et al., who were not able to associate this small semicircle with any distinct phenomenon.[19] Thus, we selected an equivalent circuit made of resistors (R) and constant phase elements (CPE), which represent the resistive and the non-ideal capacitive contributions of each phenomenon. Specifically, the equivalent circuit R$_0$(R$_{gb}$CPE$_{gb}$)(R$_{low}$CPE$_{low}$)CPE$_{el}$ depicted in Fig. 5b, was used to model the experimental data of both samples, where R$_0$ is the circuit resistance, external to the sample, R$_{gb}$ and CPE$_{gb}$ are associated with the ionic transport at grain boundaries, R$_{low}$ and CPE$_{low}$ represent the low-frequency unidentified semicircle and CPE$_{el}$ is related to the double layer capacitance of the electrodes. The accuracy of experimental data fitting is supported by Figs. S6 and S7. We can confidently exclude the presence of intra-grain contributions, since it appears as a scientific consensus that the bulk conductivity of NASICON materials can be identified only at very low temperatures, from −100 °C to 10 °C.[20–23] Moreover, the capacitive contribution of the first semicircle is equal to 10^{-9} F, which is within the typical range of grain boundary phenomena.[24] On these premises, we can evaluate the total ionic conductivity (σ), which mainly derive from the ionic transport occurring at grain boundaries for both samples. Figure 5c displays the representative Nyquist plots resulting from EIS analyses carried out at 20 °C, 50 °C and 80 °C. By fitting them, we can calculate the total ionic conductivity of both aLATP and rLATP pellets. From the resulting values, shown in Fig. 5d in the form of Arrhenius plot, aLATP appears more conductive than rLATP throughout the temperature range. The slope of the Arrhenius plot expressed in the linear form $\ln(\sigma) = \ln(A) - E_a/RT$, has been used to calculate the activation energy, which corresponds to 0.44 (±0.01) eV and 0.40 (±0.02) eV for aLATP and rLATP, respectively (Table I). Both values are in good agreement with those reported in the literature.[23,25] The ionic conductivity of aLATP at 20 °C is equal to 1.5×10^{-4} S cm^{-1}, about twice that of rLATP (8.5×10^{-5} S cm^{-1}). This difference is mainly due to a less efficient ionic conduction at the grain boundaries of rLATP. The origin of this different contribution could be related to a slightly different morphology of the particles. As discussed above, no significant differences in the morphology of the crystallites of the two samples have been observed. However, as displayed in Fig. 1, aLATP crystallites appear slightly more uniform in the shape, which could be beneficial to achieve a tighter packing.

To verify this hypothesis, we acquired cross-section SEM images on both aLATP and rLATP hot-pressed pellets. At low magnification (Figs. 6a, 6b), we did not observe any significant difference between the two pellets. Hence, we acquired high magnification images by selecting the most representative areas of both samples.
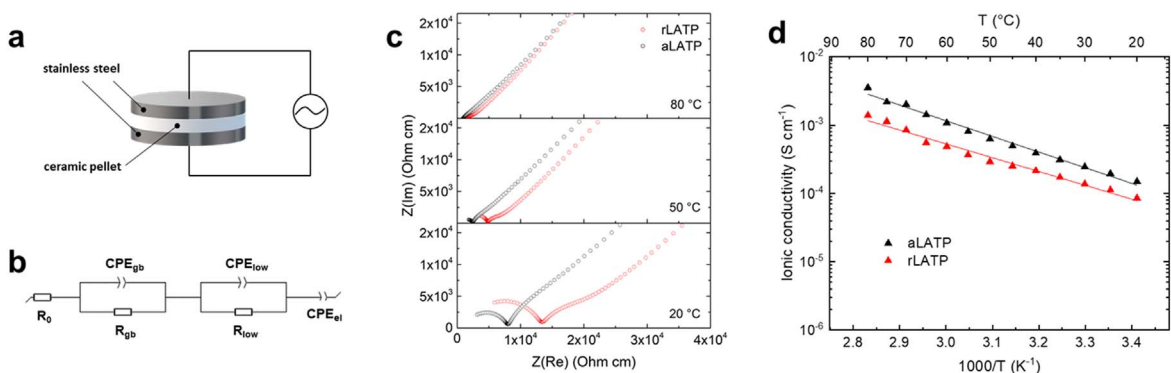

Figure 5. (a) Scheme of the setup used for EIS analysis of aLATP and rLATP. (b) Equivalent circuit used for EIS data fitting. Representative (c) EIS spectra at 20 °C, 50 °C and 80 °C and (d) Arrhenius plot in a temperature range of 20 °C–80 °C of aLATP and rLATP.

Table I. Average grain size, density and ionic conductivity with corresponding activation energy measured at 20 °C of aLATP and rLATP pellets.

Sample	Average grain size (Å)	Density	σ (S cm^{-1})	E_a (eV)
aLATP	76	90%	1.5×10^{-4}	0.44 (±0.01)
rLATP	197	90%	8.5×10^{-5}	0.40 (±0.02)
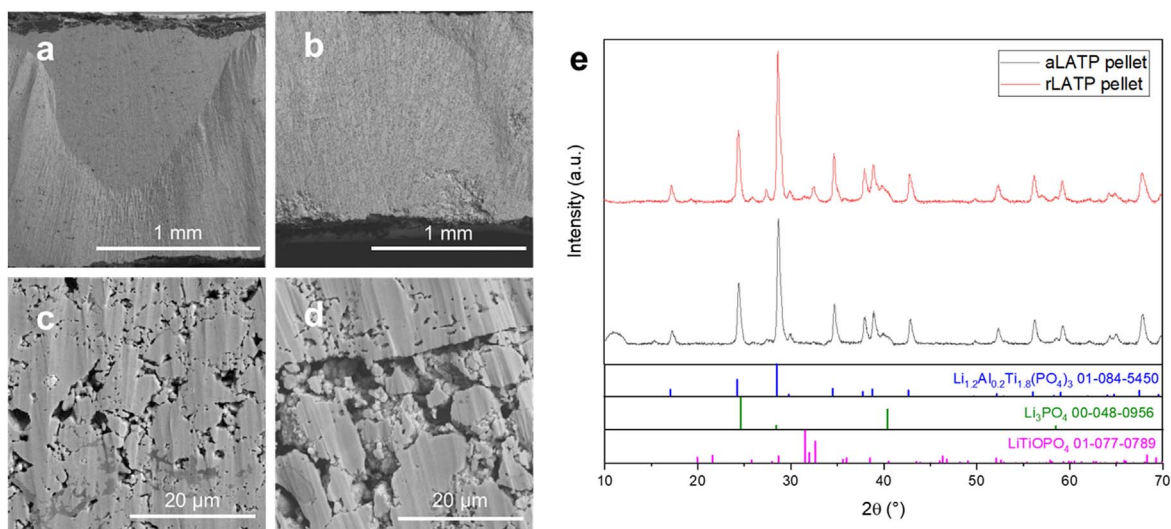
Figure 6. Cross-section SEM images of (a), (c) aLATP and (b), (d) rLATP pellets densified at 750 °C by hot-pressing, acquired after EIS analyses, and (e) corresponding XRD patterns.

This allowed us to estimate the local porosity of the pellets, which is strongly related to the effectiveness of the densification process. Moreover, we can observe the presence of fractures, which are detrimental for the achievement of fast ionic conduction. After investigating several areas of both samples, the most representative ones are shown in Figs. 6c, 6d. While the local porosity is similar in both samples, i.e. 9%–10%, which well correlates with the pellets' density, aLATP densification appears more uniform, which ensures a better contact between particles and consequently a more effective Li conduction at the interface. Meanwhile, rLATP is characterized by fractures and larger pores, probably arising from a less efficient packing of the particles during the hot-pressing step. Pores and fractures could stem from the different average particle size calculated from the diffraction data of the pellets. In fact, rLATP is characterized by slightly bigger particles (Table I), which can negatively affect its densification process. This phenomenon generates several bottlenecks along the path of Li ions, thus slowing down their transport between the electrodes and negatively affecting the final conductivity of the rLATP pellet. To exclude any potential influence of pellets' composition on the ionic conductivity values, we acquired XRD patterns of both aLATP and rLATP pellets (Fig. 6e). We did not observe any unexpected evolution of LATP peaks, however peaks associated with the impurity phases of LiTiOPO$_4$ and Li$_3$PO$_4$ were detected in both samples. The peaks appear slightly more intense in the rLATP pattern, which correlates well with its low ionic conductivity measured by EIS. Hupfer et al. reported that small percentages of LiTiOPO$_4$ can be beneficial for the ionic conductivity of LATP, especially when low sintering temperatures are used[26]; however, this phenomenon was observed with the simultaneous presence of AlPO$_4$ impurity phase, which we did not detect. Since, in our study, both aLATP and rLATP display a similar composition, we can assert that the main contribution to the difference observed in the ionic conductivity behavior is presumably associated with their morphology as demonstrated by cross-section SEM analysis.

Conclusions

In summary, we investigated the effects of anatase and rutile as Ti source for the solid-state synthesis of a LATP electrolyte. From a morphological point of view, no significant differences were observed in the crystallites of the prepared samples. The crystallization of LATP has been studied by in situ HTXRD. We observed that aLATP starts forming at a lower temperature while rLATP displays less impurity phases. After hot-pressing the corresponding powders, the ionic conductivity of the densified pellets has been measured: aLATP has a higher conductivity, mainly because of a lower grain boundary resistance. Hence, anatase TiO$_2$ should be chosen for lower synthesis temperature and higher conductivity, while rutile TiO$_2$ is the choice for purer crystals.

Current trends focus on optimizing known solid electrolyte materials rather than searching for alternatives. In this framework, every achievement and detail, e.g. selecting the best precursor materials as well as the proper synthesis temperature, can be helpful to lower the cost and improve the current methods. This aspect is crucial for the industrial scale up of solid electrolyte synthesis, which is a mandatory step for the future deployment of all-solid-state batteries. We thus believe that our findings can represent an important contribution towards the development of more efficient and less expensive syntheses for Ti-based solid electrolytes.

ORCID

Andrea La Monaca https://orcid.org/0000-0001-5511-6586
Wen Zhu https://orcid.org/0000-0003-0175-5686

Zimin Feng ⓘ https://orcid.org/0000-0002-2751-2933
Giovanni Bertoni ⓘ https://orcid.org/0000-0001-6424-9102
Daniele Campanella ⓘ https://orcid.org/0000-0002-3188-0819
Hendrix Demers ⓘ https://orcid.org/0000-0001-9069-9414
Andrea Paolella ⓘ https://orcid.org/0000-0002-4915-0064

References

1. J.-M. Tarascon and M. Armand, *Nature*, **414**, 359 (2001).
2. M. Armand and J.-M. Tarascon, *Nature*, **451**, 652 (2008).
3. J. B. Goodenough and Y. Kim, *Chem. Mater.*, **22**, 587 (2010).
4. M. Armand et al., *J. Power Sources*, **479**, 228708 (2020).
5. J. Janek and W. G. Zeier, *Nat. Energy*, **1**, 16141 (2016).
6. Z. Zeng et al., *Nat. Energy*, **3**, 674 (2018).
7. D. Lin, Y. Liu, and Y. Cui, *Nat. Nanotechnol.*, **12**, 194 (2017).
8. J. C. Bachman et al., *Chem. Rev.*, **116**, 140 (2016).
9. S. Chen, D. Xie, G. Liu, J. P. Mwizerwa, Q. Zhang, Y. Zhao, X. Xu, and X. Yao, *Energy Storage Mater.*, **14**, 58 (2018).
10. T. Famprikis, P. Canepa, J. A. Dawson, M. S. Islam, and C. Masquelier, *Nat. Mater.*, **18**, 1278 (2019).
11. H. Aono, E. Sugimoto, Y. Sadaoka, N. Imanaka, and G. Y. Adachi, *J. Electrochem. Soc.*, **137**, 1023 (1990).
12. R. DeWees and H. Wang, *ChemSusChem*, **12**, 3713 (2019).
13. A. Rossbach, F. Tietz, and S. Grieshammer, *J. Power Sources*, **391**, 1 (2018).
14. M. Hou, F. Liang, K. Chen, Y. Dai, and D. Xue, *Nanotechnology*, **31**, 132003 (2020).
15. J. Schnell, T. Günther, T. Knoche, C. Vieider, L. Köhler, A. Just, M. Keller, S. Passerini, and G. Reinhart, *J. Power Sources*, **382**, 160 (2018).
16. K. G. Schell, E. C. Bucharsky, F. Lemke, and M. J. Hoffmann, *Ionics (Kiel).*, **23**, 821 (2017).
17. E. J. Yi, K. Y. Yoon, H. A. Jung, T. Nakayama, M. J. Ji, and H. Hwang, *Appl. Surf. Sci.*, **473**, 622 (2019).
18. M. W. Chase, "NIST-JANAF thermochemical tables." *J. Phys. Chem. Ref. Data* 4th ed. (1998).
19. W. E. Tenhaeff, E. Rangasamy, Y. Wang, A. P. Sokolov, J. Wolfenstine, J. Sakamoto, and N. J. Dudney, *ChemElectroChem*, **1**, 375 (2014).
20. S. Breuer, D. Prutsch, Q. Ma, V. Epp, F. Preishuber-Pflügl, F. Tietz, and M. Wilkening, *J. Mater. Chem. A*, **3**, 21343 (2015).
21. J. S. Thokchom and B. Kumar, *J. Power Sources*, **195**, 2870 (2010).
22. A. Kubanska, L. Castro, L. Tortet, O. Schäf, M. Dollé, and R. Bouchet, *Solid State Ionics*, **266**, 44 (2014).
23. M. Pogosova, I. Krasnikova, A. Sergeev, A. Zhugayevych, and K. Stevenson, *J. Power Sources*, **448**, 227367 (2020).
24. Z. Huang, L. Chen, B. Huang, B. Xu, G. Shao, H. Wang, Y. Li, and C.-A. Wang*, *ACS Appl. Mater. Interfaces*, **12**, 56118 (2020).
25. Q. Xu, C.-L. Tsai, D. Song, S. Basak, H. Kungl, H. Tempel, F. Hausen, S. Yu, and R.-A. Eichel, *J. Power Sources*, **492**, 229631 (2021).
26. T. Hupfer, E. C. Bucharsky, K. G. Schell, and M. J. Hoffmann, *Solid State Ionics*, **302**, 49 (2017).